In-situ Candidates in the Stellar Halo of NGC 253

JOSIAH SHERK[1], BENJAMIN HARMSEN[1], and ERIC F. BELL[1]

[1] *University of Michigan Department of Astronomy*

April 2021

ABSTRACT

We use empirical methods to map density profiles of Red Giant Branch (RGB) populations in the stellar halo of NGC 253 with data from the Galaxy Halos, Outer Discs, Substructure, Thick Discs, Star Clusters (GHOSTS) survey. ΛCDM simulations predict smooth inner halos ($\leq$ 20 kpc) with significant populations of *in-situ* stars, which are expected to bear observable physical and chemical signatures (Pillepich et al. 2015; Cook et al. 2016). The span of *in-situ* formation histories, varying mechanisms of formation, and infall of accreted stars leads to a variety of chemical signatures that can make it difficult to separate individual stars into the two categories (Pillepich et al. 2015). On average, *in-situ* populations are younger and have higher median metallicity than accreted populations (Font et al. 2011; Monachesi et al. 2019). We focus our analysis on the inner halo ($\leq$20 kpc) of NGC 253, where we detect a steep density profile (power law with α= -2.48) of metal-rich stars ([M/H]$\in$(-0.50,0.00)). We contend this selection of stars is a candidate for an in-situ population.

1. INTRODUCTION

1.1. ΛCDM Simulations and Stellar Halos

The Dark Energy + Cold Dark Matter (ΛCDM) paradigm explains the heirarchical formation of large structures in the universe (White & Reese 1978; Searle & Zinn 1978; Springel et al. 2005; Reid et al. 2010), but the mechanisms that form smaller structures such as galaxies are not fully understood (Cook et al. 2016; Bullock and Boylan-Kolchin 2017). Recent work suggests galaxies form through a combination of heirarchical and dissipative processes, leaving behind observable physical and chemical signatures in the stellar halo (Zolotov et al. 2009; Cooper et al. 2015; Pillepich et al. 2015; Monachesi et al 2016). With increasing progress in the ability to resolve stellar halos (Cook et al. 2016; Monachesi et al. 2016), models with higher resolution are needed to explain observations and offer more precise predictions.

Resolution and model complexity vary in each of three commonly used types of ΛCDM Hydrodynamical simulations. There are Smooth Particle Hydrodynamics (SPH) + N-body simulations (*Eris, Eagle*) that model large 3d volumes and their interactions with gas particles (Zolotov et al. 2009; Font et al. 2011; Guedes et al. 2011; Pillepich et al. 2015). At the end of each run, many of these divisions are empty or near empty, necessitating the scale of the plane to be adapted.

There are also N-body models that use particle tagging and/or semi-analytic approaches (*Aquarius*+GALFORM) to enhance spatial and particle resolution by tagging particles and/or simplifying processes such as supernovae feedback, gas cooling rates, and star formation (Kauffmann et al. 1999; Springel et al. 2001; Helly et al. 2003; Hatton et al. 2003; Kang et al. 2005; Bower et al. 2006; De Lucia et al. 2006; Bullock and Johnston 2005; Cooper et al. 2010).

Lagrangian mesh simulations (*Illustris, IllustrisTNG, Auriga*) model non-gas particles and implement the AREPO subroutine, which improves resolution by using a Vornoi Tesselation to transform the 3d coordinate system at each time step, minimizing the computing power used on empty space (Cooper et al. 2015; Cook et al. 2016; Monachesi et al. 2016b; Pillepich et al. 2017; Monachesi et al. 2019). Literature in each of the above techniques suggests that stellar halos assemble through two mechanisms: the accretion of material from satellites and formation of stars in the halo of the progenitor.

The latter, loosely defined as *in-situ* stars, form in the Dark Matter (DM) Halo of the progenitor. Hydrodynamical simulations (Kauffmann et al. 1999; Springel et al. 2001; Helly et al. 2003; Hatton et al. 2003; Kang et al. 2005; Bower et al. 2006; De Lucia et al. 2006; Bullock and Johnston 2005; Zolotov et al. 2009; Cooper et al. 2010; Guedes et al. 2011; Font et al. 2011; Cooper et al. 2015; Pillepich et al. 2015; Cook et al. 2016; Pillepich et al. 2017) predict that these *in-situ* stars should be numerous and dominate the mass fraction of the inner halo ($\leq$20 kpc). While simulations can ascertain these populations with particle-tagging techniques, it is difficult to differentiate a halo's *in-situ* and *ex-situ* components in observations as the chemical signatures of the two populations can overlap.

Cooper et al. 2015 classified in-situ stars into three

categories: 1) stars formed in cold gas regions of the inner halo 2) stars formed from gas stripped from satellites and 3) stars formed in the thin disc and were ejected through tidal interactions during mergers.

Stars formed in regions of cold gas in the inner halo are less numerous, and feedback mechanisms such as stellar winds can remove metals more efficiently here than in the disc (Cook et al. 2016). All else held constant, this can result in a steeply negative metallicity and density profile between the disc and the outer boundary of the inner halo (Font et al. 2011; Cooper et al. 2015; Cook et al. 2016). Stars accreted from satellite galaxies are likely to bear the metallicity signatures of their progenitor, which can dominate the outer halo and is relatively metal-poor (∼1/10 solar metallicity) (Font et al. 2011; Deason et al. 2016, D'Souza & Bell 2018). Moreover, gas stripped from satellites will bear the chemical signatures of accreted stars, making the two types difficult to differentiate. In-situ stars formed in the disc, however, are likely to exhibit chemical properties similar to the disc and are expected to be relatively metal-rich (∼1/3 solar) (Font et al. 2011; Cook et al. 2016).

These predictions are applicable to spherically averaged metallicity and density profiles. In observations, spherically averaged profiles may lead to unwanted contamination from the disc along the major axis (Harmsen et al. 2017), so we use minor axis observations in this work. However, taking observations along the minor axis systematically remove some of the contributions of *in-situ* populations, making their detection more difficult (Monachesi et al. 2019).

1.2. The GHOSTS Survey

The GHOSTS survey is one of the largest studies of nearby galactic outskirts to date, individually resolving sources in 16 high-mass spiral galaxies within 17 Mpc (Radburn-Smith et al. 2011). Each galaxy contains highly resolved patches taken with the Hubble Space Telescope (HST) ACS/WFC3 cameras. Previous literature has used the survey to construct metallicity and density profiles of nearby stellar halos (Bailin et al. 2011; Monachesi et al. 2013; Streich et al. 2014; Monachesi et al. 2015; Monachesi et al. 2016; Harmsen et al. 2017). Notably, RGB populations dominate the GHOSTS fields, vary in metallicity, and are easy to see on a Color-Magnitude Diagram (CMD) - making them easy to use as tracer stars (Radburn-Smith et al. 2011; Harmsen et al. 2017).

1.3. NGC 253

Within the GHOSTS survey, NGC 253 is favorable for the study of stellar halos as it is an edge-on galaxy. This feature has allowed HST to individually resolve stars along both the major and minor axes. NGC 253 is a starburst nucleus galaxy (SBNG) with a strong stellar wind powered by its central starburst (Mouhcine et al. 2002; Comerón et al. 2002) and an oblate halo with axis ratio $\sim 0.35 \pm 0.1$ (Bailin et al. 2011). The direction of NGC 253 (00h 47m 33.10s, -25d 17m 17.6s) has an extinction of $A_v \sim 0.6$ mag (Radburn-Smith 2011). While many ΛCDM simulations suggest that stellar halos should have steeply negative spherically averaged metallicity profiles, Monachesi et al. 2016 found that NGC 253 has a relatively flat metallicity profile (see Table 1).

NGC 253 has a median halo metallicity of [Fe/H]∼-1.05 (out to 80 kpc) (Monachesi et al. 2016). The metallicity of the disc has previously been assumed to be solar (Davidge 2016) and is difficult to ascertain as the disc of NGC 253 has a significant amount of dust.

Property	Value	Units
T. Stel. Mass[a]	$5.5\pm1.4\text{x}10^{10}$	$M_\odot$
T. Stel. Halo Mass[a]	$4.53^{+0.53}_{-0.31}\text{x}10^{9}$	$M_\odot$
Color Gradient[b]	-7.0±6.1	10^{-4}mag kpc^{-1}

Table 1: Properties of NGC 253. T. is abbreviation for Total, Stel. is abbreviation for Stellar. *a: Harmsen et al. 2017. b: Monachesi et al. 2016.*

For this work, we map RGB density profiles ∈∼(4,40) kpc by metallicity in search of *in-situ* population signatures. We consider RGB populations along the minor axis of NGC 253. In Section 2, we discuss the methods we use to reduce the data, including foreground subtraction, artificial star tests, and background subtraction. In Section 3, we present power-law relationships for each density profile and star count fractions of the RGBs by metallicity. In Section 4, we discuss four potential interpretations of our findings and future work.

2. METHODS

2.1. Photometry and CMD Cut Selection

Within the Hubble Archive, there are files for 20 fields measured along the major and minor axes of NGC 253, each containing the following information for individually resolved objects: extinction-corrected magnitudes in the F606W and F814W filters, RA, DEC, and x / y pixel coordinates on the HST ACS/WFC camera. In this study we focus solely on the minor axis fields, which are fields 8, 11, 12, 13, 14, 15, 16, 17, 18, 19, and 20.

We use the same reduced FITS files, masks, and Artificial Star Tests (ASTs) (Radburn-Smith 2011) as Harmsen et al. 2017, where we refer the interested reader. In this work we use RGB stars as tracers for NGC 253's stellar halo because of their well defined shape on a CMD, luminosity, and high star counts in the GHOSTS fields (Harmsen et al. 2017). We filter out foreground stars using masked FITS files and

subtract their area from each field. We proceed to construct a composite CMD of all fields and fit to 10 Gyr isochrones from the CMD 3.4 database (Figure 2) (Bressan et al. 2012,; Chen et al 2014; Tang et al. 2014; Chen et al. 2015; Marigo et al. 2017; Pastorelli al. 2019; Pastorelli al. 2020). We find that isochrone median color is less affected by shifts in age than metallicity (+0.282 mag for a +1.75 dex [M/H] shift and -0.085 mag for a -5 Gyr shift) and assume a 10Gyr age for the RGB population (Radburn-Smith et al. 2011). Subsequent plots and metallicity analysis are based off of this assumption.

We define the Tip of the Red Giant Branch (TRGB) as 23.6 mag (Harmsen et al. 2017) and set a noise cutoff for our selection at 25.5 mag (Figure 2). The RGBs are divided into four metallicity bins: [M/H]∈(-1.75,-1.20),[M/H]∈(-1.20,-0.75),[M/H]∈(-0.75,-0.50), and [M/H]∈(-0.50,0.00). We consider the first two selections to be "metal-poor" and the second two to be "metal-rich."

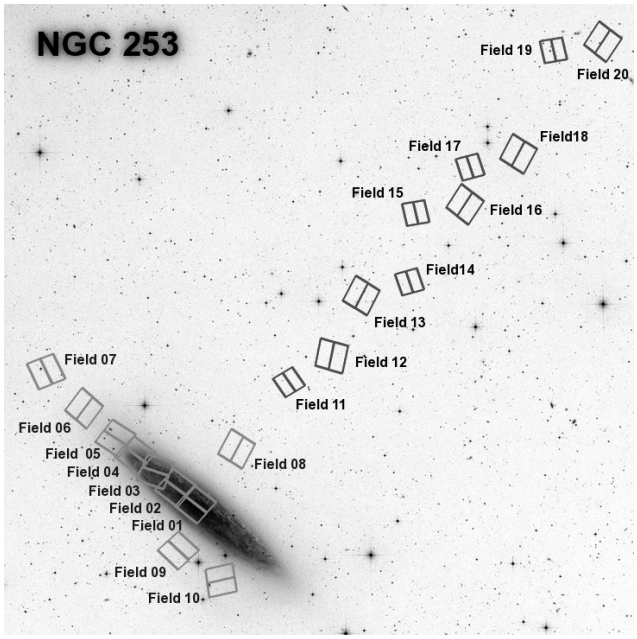

Figure 1: HST image of NGC 253 with GHOSTS fields along the major and minor axes from GHOSTS website. http://vo.aip.de/ghosts/survey.html

2.2. Artificial Star Tests

We use ASTs from the data release paper Radburn-Smith 2011. The DOLPHOT package was used to inject 500,000 to 2,000,000 artificial stars (with color and brightness similar to the observed stars) into each field. The percentage of recovered stars, as a function of magnitude, was converted into a ratio ≥ 1 by which to weight each star, accounting for overcrowding effects in bright regions.

2.3. Foreground Contamination

Using the spatial resolution of the WFC3 and ACS cameras from the HST website, we derive the area of each field and subtract foreground sources from the masks files. Depending on the number of stars that can be recovered (more stars fields closer to the disc) we slice each field into subfields and find the density for each. We find errorbars for each point with a standard 84% poisson (one sigma) confidence interval.

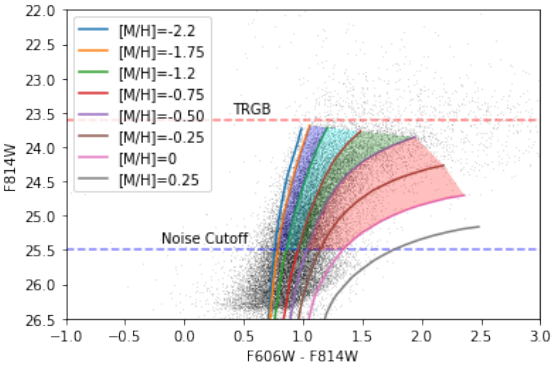

Figure 2: Composite CMD of minor axis stars in NGC 253 with fitted isochrones from the CMD 3.4 database (Bressan et al. 2012,; Chen et al 2014; Tang et al. 2014; Chen et al. 2015; Marigo et al. 2017; Pastorelli al. 2019; Pastorelli al. 2020). TRGB and Noise Cutoff are shown - with the Noise Cutoff set above a color dispersion of stars to avoid contamination in the higher metallicity cuts.

2.4. Background Subtraction

In log-log space, the resulting plots show a clear power law relationship until the profile flattens at 46.58 kpc (Figure 3). The FITS files we use have been culled (Radburn-Smith 2011) and an estimated ∼95% of contaminants have already been removed. The flattening profile is likely due to background galaxies that were not removed in the culling process. Treating these objects as background, we subtract the mean stellar density of these fields (15-20) from all other fields, limiting our radius of measurement to 36.13 kpc (maximum distance from the galactic center of field 14), allowing us to closely examine the inner halo and parts of the outer halo. Our background selection is larger than Harmsen et al. 2017, which assumes fields 18-20 as background. We note that the lack of profile steepness and RGB shape in color-mag space is not a conclusive way to ascertain background objects and cannot rule out the possibility that we have oversubtracted background contaminants.

3. RESULTS

3.1. Density Profiles

We analyze the steepness of each density profile by fitting a bootstrapped linear regression each log-log plot. We assume stellar density at radius r $log_{10}\Sigma(r)$ is drawn from a normal distribution centered about the expected density at that radius $log_{10}\Sigma'(r)$ (Harmsen et al. 2017):

$$P(log_{10}\Sigma(r)) = \frac{1}{\sqrt{2\pi}\sigma} e^{-\frac{[]log_{10}\Sigma(r) - log_{10}\Sigma'(r)]^2}{2\sigma^2}} \quad (1)$$

Our observations, which represent a sample of the true RGB popluation, account for the expected density component $log_{10}\Sigma'(r)$. We use a linear regression (with less parameters than Harmsen et al. 2016, which depends on the weighted average distance the minor axis fields r_0) in the below form, where α comes from the power law relationship $\Sigma(r) \sim r^{\alpha}$:

$$log_{10}\Sigma'(r) = log_{10}\Sigma_0 + \alpha log_{10}\Sigma(r) \quad (2)$$

We regress log radius on log density for three radial selections: $log_{10}(r) \in (0.6, 1.6)$, $log_{10}(r) \in (0.6, 1.2)$, and $log_{10}(r) \in (1.2, 1.6)$. The profiles can be approximated as linear, which we capture in the first selection, but grow steeper as they approach the galactic center, which is captured in the second selection. The third selection provides a reference point to compare the steepness of the profiles at various radii.

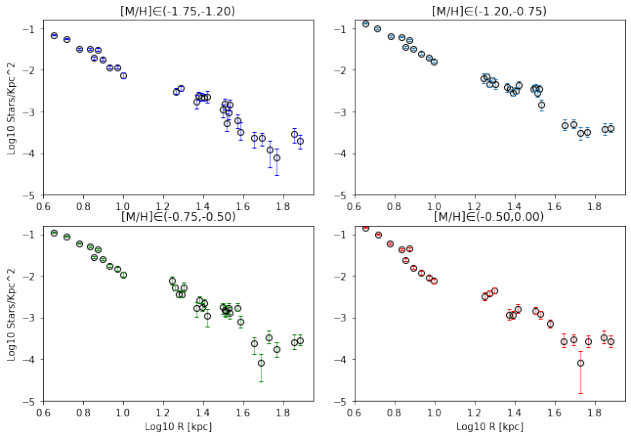

Figure 3: RGB log-log density profiles by metallicity. Suggestive of uniform density at roughly 46.58 kpc, especially in [M/H]∈(-1.20,-0.75) and [M/H]∈(-0.50,0.00) cuts.

We find that over the full radius of ∼40 kpc profiles for all four metallicity selections are steeply negative. The highest star counts are found in [M/H]∈(-1.20,-0.75), and the lowest in the cuts on the outer boundaries ([M/H]∈(-1.75,-1.20) and [M/H]∈(-0.50,0.00)). For all metallicity selections, the profiles do indeed become steeper as they approach the galactic center. Across all radial selections, the [M/H]∈(-0.75,-0.50) and [M/H]∈(-0.50,0.00) cuts are steeper than the other cuts and similar, with the exception of the radial selection within 10 kpc, where the α of [M/H]∈(-0.50,0.00) is 1 unit smaller than that of the [M/H]∈(-0.75,-0.50) selection.

While these profiles have not been spherically averaged, they were taken along the minor axis at both sides of the galactic disc. Fields 9 and 10 in particular is at a different side of the disc than the other minor axis fields. It is possible that the observed steepness in the profiles over the smaller radius (which only includes fields 9 and 8, respectively) is an artifact of halo substructure that is not accounted for. This weights the radial selection $log_{10}(r) \in (1.2, 1.6)$ with high importance as it measures fields on the same side of the disc. We note that the metal-rich cuts in this profile are still considerably steeper than the metal-poor.

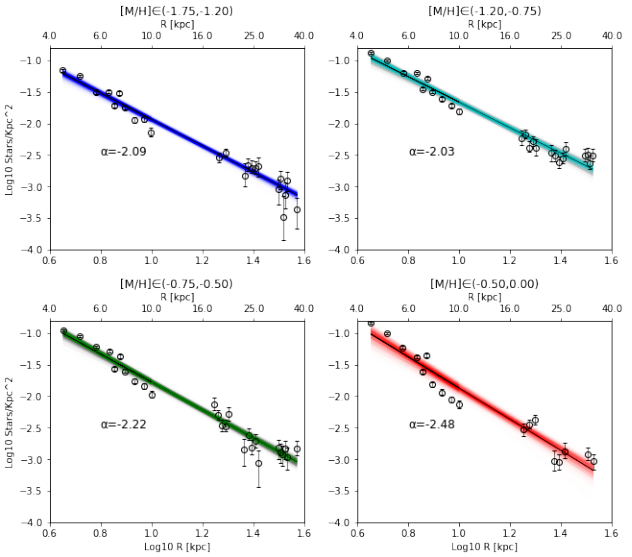

Figure 4: RGB log-log density profiles by metallicity fitted to power law line over 40 kpc radius. A simple linear regression was fit to the data along with 1100 bootstrapped regressions (shown in transparent colors blue, cyan, green, and red respectively). The confidence intervals in Table 2 are from the bootstrapped regression. Note that the radius includes and extends beyond the inner halo.

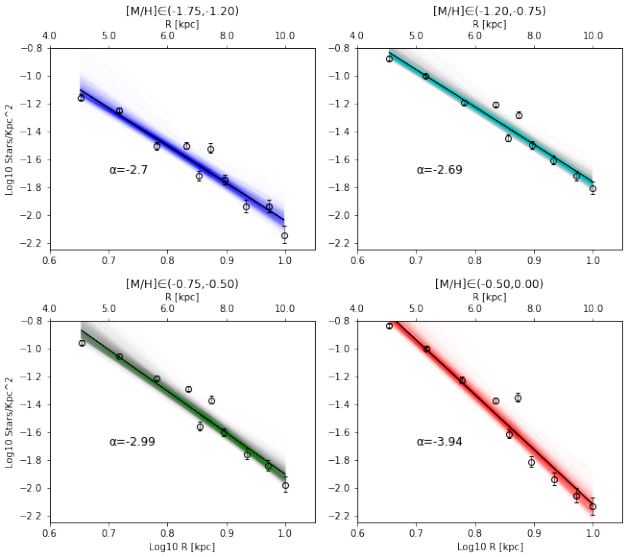

Figure 5: RGB Log-Log Density profiles by metallicity fitted to power law line over 10 kpc radius. The same regression and bootstrapping methods from Figure 4 were applied. Note that the radius extends only to fields within the boundaries of the inner halo.

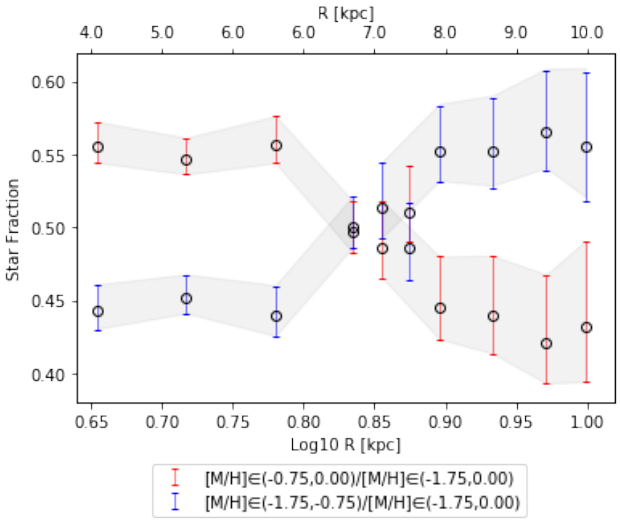

Figure 6: Star count fraction (a proxy for mass fraction) of metal-rich and metal-poor cuts over 10 kpc (part of the inner halo).

$log_{10}(r)$	$[M/H]$	$log_{10}\Sigma_0$	α
(0.6,1.2)	(-1.75,-1.20)	$0.66^{+0.23}_{-0.16}$	$-2.70^{+0.19}_{-0.27}$
–	(-1.20,-0.75)	$0.93^{+0.14}_{-0.09}$	$-2.69^{+0.11}_{-0.17}$
–	(-0.75,-0.50)	$1.09^{+0.30}_{-0.18}$	$-2.99^{+0.20}_{-0.34}$
–	(-0.50,0.00)	$1.82^{+0.30}_{-0.13}$	$-3.94^{+0.17}_{-0.35}$
(1.2,1.6)	(-1.75,-1.20)	$-0.19^{+0.29}_{-0.35}$	$-1.81^{+0.25}_{-0.48}$
–	(-1.20,-0.75)	$-0.70^{+0.44}_{-0.45}$	$-1.26^{+0.32}_{-0.32}$
–	(-0.75,-0.50)	$0.81^{+0.43}_{-0.42}$	$-2.48^{+0.29}_{-0.31}$
–	(-0.50,0.00)	$0.79^{+1.74}_{-0.68}$	$-2.51^{+0.53}_{-1.32}$
(0.6,1.6)	(-1.75,-1.20)	$0.16^{+0.08}_{-0.09}$	$-2.09^{+0.07}_{-0.07}$
–	(-1.20,-0.75)	$0.36^{+0.11}_{-0.10}$	$-2.03^{+0.09}_{-0.09}$
–	(-0.75,-0.50)	$0.45^{+0.08}_{-0.10}$	$-2.22^{+0.09}_{-0.08}$
–	(-0.50,0.00)	$0.60^{+0.16}_{-0.18}$	$-2.48^{+0.17}_{-0.14}$

Table 2: Results from bootstrapped linear regression on log-log density profiles across metallicity cuts.

3.2. Star Count Fractions by Metallicity

In addition to assessing the chemical properties and spatial distributions of the RGBs, we analyze the star count fraction (proxy for stellar mass fraction) as a function of radius. Pillepich et al. 2015 finds that the mass fraction of in-situ stars is expected to dominate the part of the inner halo (we refer the interested reader to Figure 4 of Pillepich et al. 2015). To increase the precision of our ratios (increasing star count and therefore limiting error propagation), we combine the metal-rich and metal-poor cuts into their own selections. We find that the metal-rich stars dominate the star count fraction within 10 kpc, the same radial selection that produced the steepest profiles for the metal-rich stars.

4. DISCUSSION

In Section 1 we discussed two mechanisms (*in-situ* and *ex-situ* star formation) that form stellar halos and the signatures they leave behind. We established that ΛCDM simulations suggest there should be a significant *in-situ* component to stellar halos, which should have an observably steep density profile, high median metallicity, and dominate the mass fraction in the inner halo. When binning RGB selections by metallicity, we observe the steepest density profiles in our metal-rich selections ([M/H]∈(-0.75,-0.50) and [M/H]∈(-0.50,0.00)) and find that these populations dominate the star count fraction up to ∼6 kpc.

We will discuss four plausible explanations for the population of metal-rich RGBs: 1) that they are background galaxies, which we rule out 2) that they are metal-rich accreted stars 3) that they are *in-situ* stars that formed in the inner halo and 4) that they are *in-situ* stars that formed in the disc.

4.1. Metal-rich RGBs as Background Galaxies

There is no consensus on how to properly select background galaxies from CMDs and subtract them from star counts. The process involves some trial and error as subtraction propagates errors, increasing the uncertainty in each measurement. It is possible to oversubtract or undersubtract background from a CMD, thereby facing greater star count uncertainties and failing to measure actual stars in the case of oversubtraction, and interpreting background galaxies as halo substructure in the case of undersubtraction. We select background fields based on a flattening of the power law profile at 46.58 kpc, which is a signature of uniformly distributed objects. Our background level is the mean of star counts from five fields as our background level, which includes fields with higher star counts than prior work (Harmsen et al. 2017), meaning it is more likely we oversubtracted than undersubtracted these objects, leading to higher measurement uncertainties (reflected in one sigma poisson error bars) than incorrect interpretation of background objects. Moreover, we know the distribution of background galaxies to be relatively uniform in both kpc and color-mag space. We would expect galaxies at this brightness (23.5-25.5 mag) to be relatively blue, while our sources in the metal-rich cuts are more red. At a radius of ∼6 kpc, the observed objects are ∼100x more dense than the uniformly distributed background objects we observe in the outer fields (fields 15-20). Therefore, we reject that the steepening power law in the inner halo is due to background galaxies.

4.2. Metal-rich RGBs as Accreted Stars

It is possible our metal-rich selections are indeed RGBs but do not represent an *in-situ* component to the stellar halo. Hydrodynamical simulations predict accreted stars falling into the disc over the lifetime of

a galaxy, making up ∼23% of its stellar mass when enough time has passed since the most recent merger (Pillepich et al. 2015). Moreover, tidal interactions from mergers will displace *in-situ* stars that formed in the disc and inner halo, making it difficult to distinguish between the two populations based on spatial distribution alone. Our assumption that *in-situ* stars exhibit higher metallicity is based on the central tendency of the Metallicity Distribution Function (MDF) for such a population (Font et al. 2011; Pillepich et al. 2015; Monachesi et al. 2019), where the tails of *in-situ* and *ex-situ* MDFs overlap and can make it difficult to distinguish the two based on chemical properties alone. While it is possible for accreted halos to bear negative metallicity gradients, this is more common if such a gradient reflects the behavior of the rest of the outer halo on the minor axis ≥20 kpc (e.g. see Monachesi et al. 2019, which simulated minor axis profiles ∈(10,120) kpc, which excludes most of our inner sample), which we know to be flat in NGC 253 (Monachesi et al. 2016). If our metal-rich RGB selections are indeed accreted stars, they would have needed enough time since the most recent merger to fall into the disc and produce such a steep profile. We differ the analysis of the timeline of the most recent merger to future work, which might be compared to the star count fractions observed to provide evidence for the feasibility of this explanation.

4.3. Metal-rich RGBs as In-situ Stars Formed in the Inner Halo

If the RGBs formed in the inner halo, there are two mechanisms by which they may have formed: 1) with gas from the progenitor 2) with gas stripped from infalling satellites (Cook et al. 2016). While the spatial distributions of each type are similar, the chemical signatures differ. If the stars formed with gas from the progenitor - they would have formed in a low density region with similar metallicity to the disc. If they formed from the gas of an infalling satellite, however, they would likely bear the chemical signature of the satellite and be very difficult to distinguish from accreted stars in metallicity space. We contend that these metal-rich stars were not formed *in-situ* with stripped gas from infalling satellites but cannot rule out that they may be *in-situ* stars that formed in the cold gas regions of the progenitor's inner halo.

4.4. Metal-rich RGBs as In-situ Stars Formed in the Disc

The metal-rich RGB population may have formed in the disc of NGC 253 before these stars were ejected into the inner halo through tidal interactions during mergers. Hydrodynamical simulations predict significantly steeper density profiles for these "heated disc" *in-situ* stars than for stars formed in the halo or accreted from satellites (Font et al. 2011; Cooper et al. 2015). The median metallicity of this population would be similar to that of the disc (although not exactly the same because of the wide span of stellar formation histories), which is difficult to determine in NGC 253 because of prolific amounts of dust. Previous literature (Davidge 2010) has assumed solar metallicity for the disc, which may very well be an overestimate of the true value. Font et al. 2011 predicts metallicity $\leq \sim \frac{1}{3}$ solar for such stars, which is very similar to the population we observe. We contend that the two most likely explanations for the population are that they formed in the cold gas regions of NGC 253's inner halo or in the disc, before being displaced further into the halo during merger events.

4.5. Causes for Error and Additional Considerations

It is worth noting that at small radii (≤ 10 kpc), it can be difficult to discern individual stars (Monachesi et al. 2019), and our result of a star count fraction dominated by metal-rich populations occurs within 10 kpc. We contend that our artificial star tests (Radburn-Smith et al. 2011) allow us to correct star counts at these radii enough for us to interpret.

We also note that a negative metallicity gradient is predicted by Hydrodynamical models (Zolotov et al. 2009; Font et al. 2011; Cooper et al. 2015; Pillepich et al. 2015; Cook et al. 2016) to be a signature of *in-situ* star populations in stellar halos. This signature is not observed in NGC 253 but is found in several MW-mass galaxies (Monachesi et al. 2016). Why then do we focus on NGC 253 if it has a flat metallicity profile? The metallicity gradient as a function of radius is not necessarily a characteristic of either *in-situ* or *ex-situ* populations (Font et al. 2011) (although it can be in some accreted halos (Monachesi et al. 2019)), rather it is a byproduct of the transition between the two populations in the inner to outer halo. The metallicity in either population can be diverse, but the central tendencies of the MDFs suggest *in-situ* populations on average have higher median metallicities than *ex-situ*, meaning that a significant population (one which dominates the mass fraction) of *in-situ* stars in the inner halo could raise the median metallicity at that radius before it flattens to the relatively low metallicity of accreted stars in the outer halo. Our analysis shows that while relatively few metal-rich RGBs were detected over the full ∼ 80 kpc radius, they dominated the star count fraction within a ∼6 kpc radius of the inner halo. The flat metallicity gradient of NGC 253 is not a contradiction of our findings as 1)it measures color change over a broader radius and 2)the star counts of metal-rich stars are relatively low in our dataset but still dominates parts of the inner halo.

5. SUMMARY

Using data from the HST GHOSTS survey reduced with the DOLPHOT subroutine (Harmsen et al. 2017), we map density profiles of RGBs in NGC 253's stellar

halo in four metallicity cuts: [M/H]∈(-1.75,-1.20), [M/H]∈(-1.20,-0.75) [M/H]∈(-0.75,-0.50), and [M/H]∈(-0.50,0.00). Our analysis reveals that the two metal-rich selections have the steepest density profiles out to ∼40 kpc, mirroring two signatures predicted by Hydrodynamical simulations of *in-situ* star populations (high median metallicity and steep density profiles). We consider the possible origins of this population are most likely to be metal-rich *ex-situ* stars, *in-situ* stars formed in the inner halo, or *in-situ* stars formed in the disc. We defer the analysis of NGC 253's merger history and the search for *in-situ* signatures in other stellar halos to future work.

6. ACKNOWLEDGEMENTS

We would like to thank NASA for making data collection with the HST in the GHOSTS survey a possibility, as well as the authors of the CMD 3.4 database (Bressan et al. 2012,; Chen et al 2014; Tang et al. 2014; Chen et al. 2015; Marigo et al. 2017; Pastorelli al. 2019; Pastorelli al. 2020) and of the other works referenced in this letter.

7. REFERENCES

Bailen J., Bell E.F., Chappell S.M., Radburn-Smith D.J., de Jong R.S., 2011, *ApJ*, 736, 24.

Bower R.G., Benson A.J., Malbon R., Helly J.C., Frenk, C. S., Baugh C.M., Cole S., Lacey, C.G., 2006, *MNRAS*, 370, 645-655.

Bressan A., Marigo P., Girardi L., Salasnich B., Cero D., Rubele S., Nanni A., 2012, *MNRAS*, 427, 127-145.

Bullock J.S., Boylan-Kolchin M., 2017, *ARAA*, 55, 343-387.

Bullock J.S., Johnston K.V., 2005, *ApJ*, 635, 931-949.

Chen Y., Girardi L., Bressan A., Marigo P., Kong X., 2014, *MNRAS*, 444, 2525-2543.

Chen Y., Girardi L., Bressan A., Marigo P., Kong X., Lanza, A., 2015, *MNRAS*, 452, 1068.

Comerón F., Goméz A.E., Torra J., 2003, *A&A*, 400, 137-143.

Cook B.A., Conroy C., Pillepich A., Hernquist L., 2015, *IAU Symposium*, 317.

Cook B.A., Conroy C., Pillepich A., Rodriguez-Gomez V., Hernquist L., 2016, *ApJ*, 833, 158.

Cooper A.P., Cole S., Frenk C.S., White S.D.M., Helly J., Benson A.J., De Lucia G., Helmi A., Jenkins A., Navarro J.F., Springel V., Wang J, 2010, *MNRAS*, 406, 744-766.

Cooper A.P., Parry O.H., Lowing B., Cole S., Frenk C., 2015, *MNRAS*, 454, 3185-3199.

Davidge, T.J., 2010, *ApJ*, 725, 1342.

Deason A.J., Mao Y., Wechsler R.H., 2016, *ApJ*, 821, 15.

De Lucia G., Springel V., White S.D.M., Croton D., Kauffmann G., 2006, *MNRAS*, 366, 499-509.

D'Souza R., Bell E.F., 2018, *MNRAS*, 474, 5300-5318.

Font A.S., McCarthy I.G., Crain R.A., Theuns T., Schaye J., Wiersma R.P.C., Vecchia C.D., 2011, *MNRAS*, 416, 2802-2820.

Guedes J., Callegari S., Madau P., Mayer L., 2011, *ApJ*, 742, 76.

Harmsen B., Monachesi A., Bell E.F., de Jong R.S., Bailin J., Radburn-Smith D.J., Holwerda B.W., 2017, *MNRAS*, 466, 1491-1512.

Hatton S., Devriendt J.E.G., Ninin S., Bouchet F.R., Guideroni B., Vibert D., 2003, *MNRAS*, 343, 75-106.

Helly J.C., Cole S., Frenk C.S., Baugh C.M., Benson A., Lacey C., 2003, *MNRAS*, 338, 903-912.

Kang X, Mao S., Gao L., Jing Y.P., 2005, *A&A*, 437, 383-388.

Kauffmann G., Colberg J., Diaferio A., White S.D.M., 1999, *MNRAS*, 303, 188-206.

Lucero D.M., Carignan C., Elson E.C., Randriamampandry T.H., Jarrett T.H., Oosterloo T.A., Heald G.H., 2015, *MNRAS*, 450, 3935-3951.

Marigo P., Girardi L., Bressan, A., Rosenfield P., Aringer B., Chen Y., Dussin M., Nanni Ambra., Pastorelli G., Rodrigues T.S., Trabucchi M., Bladh S., Dalcanton J., Groenewegen M.A.T., Montalbán J., Wood P.R., 2017, *ApJ* 835, 77.

Merritt A., van Dokkum P., Abraham r., Zhang J., 2016, *ApJ*, 830, 62.

McCarthy I.G., Font A.S., Crain R.A., Deason A.J., Schaye J., Theuns T., 2012, *MNRAS*, 420, 2245-2262.

Mouhcine M., 2005, *ApJ*, 652, 277-282.

Mouhcine M., 2006, *ApJ*, 652, 277.

Monachesi A., Bell E.F., Radburn-Smith D.J., Bailin J., de Jong R.S., Holwerda B., Streich D., Silverstein G., *MNRAS*, 457, 1419-1446.

Monachesi A., Facundo, A.G., Grand R.J.J., Kauffmann G., Marinacci F., Pakmor R., Springel V., Frank C.S., 2016, *MNRAS*, 459, L46-L50.

Monachesi A., Gómez F.A., Grand R.J.J., Simpson C.M., Kauffmann G., Bustamante S., Marinacci F., Pakmor R., Springel V., Frenk C.S., White S.D.M., Tissera P.B., 2019, *MNRAS*, 485, 2589-2616.

Pastorelli G., Marigo P., Girardi L., Chen Y., Rubele S., Trabucchi M., Aringer B., Bladh S., Bressan A., Montalbán J., Boyer M.L., Dalcanton J., Eriksson K., Groenewegen M.A.T., Höfner S., Lebzelter T., Nanni A., Rosenfield P., Wood P.R., Cioni, M.R.L., 2019, *MNRAS*, 485, 5666-5692.

Pastorelli G., Marigo P., Girardi L., Aringer B., Chen Y., Rubele S., Trabucchi M., Aringer B., Bladh S., Bressan A., Dalcanton J., Groenewegen M.A.T., Lebzelter T., Mowlavi N., Chubb K.L., Cioni M.R.., de Grijs R., Ivanov V.D., Nanni A., van Loon J.T., 2020, *MNRAS*, 498, 3283-3301.

Percival W.J., Nichol R.C., Eisenstein D.J., Weinberg D.H., Fukugita M., Pope A.C., Schneider D.P., Szalay A.S., Vogeley M.S., Zehavi I., Bahcall N.A., Brinkmann J., Connolly A.J., Loveday J., Meiksin A., 2007, *ApJ*, 657, 51-55.

Pillepich A., Madau P., Mayer L., 2015, *ApJ*, 799, 184.

Pillepich A., Nelson D., Hernquist L., Springel V., Pakmore R., Torrey P., Weinberger R., Genel S., Naiman J.P., Marinacci F., Vogelsberger M., 2017, *MNRAS*, 475, 648-675.

Pulsoni C., Gerhard O., Arnaboldi M., Pillepich A., Nelson D., Hernquist L., Springel V., 2020, *A&A*, 641, A60.

Purcell C.W., Bullock J.S., Zentner A.R., 2008, *MNRAS*, 391, 550-558.

Radburn-Smith D.J., de Jong R.S., Seth A.C., Bailin J., Bell E.F., Brown T.M., Bullock J.S., Courteau S., Dalcanton J.J., Ferguson H.C., 2011, *ApJS*, 195,

18.
Reid B.A., Percival W.J., Eisenstein D.J., Verde L., Spergel D.N., Skibba R.A., Bahcall N.A., Budavari T., Frieman J.A., Fukugita M., Richard Gott J., Gunn J.E., Ivezíc Z., Knapp G.R., Kron R.G., Lupton R.H., McKay T.A., Meiksin A., Nichol R.C., Pope A.C., Schlegel D.J., Schneider D.P., Stoughton C., Strauss M.A., Szalay A.S., Tegmark M., Vogeley M.S., Weinberg D.H., York D.G., Zehavi I., 2010, *MNRAS*, 404, 60-85.
Searle L., Zinn R., 1978, *ApJ*, 225, 357-379.
Springel V., White S.D.M., Tormen G., Kauffmann G., 2001, *MNRAS*, 328, 726-750.
Tang J., Bressan, A., Rosenfield P., Slemer A., Marigo P., Girardi L., Bianchi L., 2014, *MNRAS*, 445, 4287.
White S.D.M., Reese M.J., 1978, *MNRAS*, 183, 341-358.
Zolotov A., Willman B., Brooks A.M., Governato F., Brook C.B., Hogg D.W., Quinn T., Stinson G., 2009, *ApJ*, 702, 1058-1067.